Facile Electrochemical Fabrication of Large-Area ZnO Inverse Opals with Reduced Defects

Yi-Jui Huang, Chen-Hong Liao, Bo-Han Huang, Wan-Ying Chen, and Pu-Wei Wu[*,z]

Department of Materials Science and Engineering, National Chiao Tung University, Hsin-Chu 300, Taiwan

We demonstrate a facile fabrication scheme to construct large-area ZnO inverse opals on an indium-tin-oxide substrate with significantly reduced defects and improved stoichiometry. The fabrication steps involve the preparation of colloidal template via vertical electrophoresis of polystyrene (PS) microspheres in 720 nm radius, followed by galvanostatic electrodeposition of ZnO in the interstitial voids among the PS microspheres. Subsequently, the sample undergoes a heat-treatment in air at 500°C for different time to remove the colloidal template, leaving an integral ZnO skeleton with thickness adjusted by the electrodeposition time. Since the colloidal template is deliberately designed with desirable thickness and considerable uniformity, the electroplating of ZnO can be achieved in a reduced ethanol/water ratio that allows faster growth rate and improved ZnO structure. Scanning electron microscope images demonstrate negligible microstructural defects for the ZnO inverse opals. X-ray diffraction reveals a wurtzite hexagonal lattice with (002) preferred orientation. In addition, both X-ray photoelectron spectroscopy and photoluminescence spectra suggest improved crystallinity and stoichiometry with increasing heat-treatment time.

Zinc oxide (ZnO) is a low-cost semiconductor material with direct wide bandgap (3.36 eV at room temperature) and large exciton binding energy (60 mV).[1] With impressive chemical stability and biological compatibility, ZnO has attracted considerable attention in recent years for possible applications in photocatalysis, electronics, photovoltaics, optoelectronics, wetting, chemical and biomolecular sensors, and so on.[2–7] To further improve its functionality and activity, ZnO is often doped with selective elements with the objective to introduce impurities for modification in both lattice and electronic configurations.[8,9] An alternative route to achieve the same purpose is to fabricate the ZnO in unique forms. For example, a rich variety of ZnO nanostructures such as nanosheets, nanowires, nanobelts, nanoplatelets, nanotubes, and inverse opals have been successfully synthesized and characterized.[10–15] Among them, the inverse opal is of particular interest because it is an integral platform that can be used directly for device fabrication, unlike those nanostructures that require a supporting substrate to deposit on.

The inverse opals are also known as three-dimensionally ordered macroporous materials (3DOM) that contain periodic submicrometer pores in a hexagonal arrangement. Conventional preparation methods for the inverse opals entail the self-assembly of SiO_2 or polystyrene (PS) microspheres via sedimentation or solvent evaporation to form a colloidal template, followed by physical, chemical, or electrochemical deposition of desirable materials into the interstitial voids among the microspheres. Afterward, the colloidal template is selectively removed by chemical dissolution or thermal burn-off, leading to the formation of periodic porous structure with interconnected skeleton. The diameter for the microspheres is often adjusted to produce 3DOM with desirable porosities. Earlier attempts to fabricate the 3DOM structures were steered toward the exploration of their unique optical responses for photonic crystals.[16–18] Later on, the 3DOM was recognized for possible applications in sensors and electrocatalysis because its excessive surface area and interconnected pores allow large reaction area and facile mass transfer over conventional planar counterparts. In general, the inverse opals can be fabricated in both planar and cylindrical forms.[19,20] To date, inverse opals of metals (Ni, Au, Co, Fe, and their alloys) and compounds (CdS, CdSe, PbO_2, IrO_2, ZnO) have been demonstrated.[21–27] A comprehensive review on the morphology control for the inverse opals is provided by Stein et al.[28] The fabrication of ZnO inverse opals has been reported in literature in which a variety of deposition methods including atomic layer deposition, chemical vapor deposition, chemical conversion, and electrophoretic deposition are evaluated with various success.[29–34] Despite these methods being able to

form ZnO inverse opals with reasonable structural integrity, exact layer-by-layer control over ZnO thickness is difficult to achieve.

Earlier, we reported that electrophoresis in a vertical arrangement facilitated the construction of large-area colloidal template with superb surface uniformity and controlled thickness in a relatively short time as compared to conventional sedimentation and solvent evaporation techniques.[35] In addition, upon immersion in suitable electrolyte, the colloidal template allowed uniform electrodeposition forming a metallic replica in a layer-by-layer mode.[36] In this work, we demonstrate a facile route (less than 4.5 h) to fabricate large-area ZnO inverse opals with reduced crystallographic defects and improved stoichiometry involving electrophoresis of PS microspheres, electroplating of ZnO, and heat-treatment to remove the PS template.

Experimental

The PS microspheres were synthesized via an emulsifier-free emulsion polymerization process in which styrene was used as the monomer after removing inhibitors and $K_2S_2O_8$ was used as the initiator. The polymerization was carried out at 70°C, resulting in the formation of PS microspheres in radius of 720 nm with a standard deviation of 16.7 nm. Details on the synthetic conditions have been reported elsewhere.[37]

To prepare the PS colloidal crystals, we adopted an electrophoretic deposition technique in a vertical arrangement with two parallel electrodes. First, the PS microspheres (1 g) were dispersed in ethanol (100 ml) with the *p*H adjusted to 8 to form a stable suspension. The substrate to be deposited was an indium-tin-oxide (ITO) glass (2 × 2 cm^2) and the counterelectrode was a stainless steel plate (7.5 × 5 cm^2). The electric field imposed for electrophoresis was 10 V/cm and the process lasted for 10 min at 26°C. Afterward, the PS colloidal crystals were carefully removed and dried in air at 50°C for 10 min rendering an integral PS template with thickness of 13 μm.

To fabricate the ZnO inverse opals, the PS colloidal crystals were immersed in a ZnO plating solution consisting of 0.1 M $Zn(NO_3)_2$ in mixture of water (90 vol %) and ethanol (10 vol %). A galvanostatic plating of 1 mA/cm^2 was applied at 70°C and its duration was adjusted to obtain ZnO with thickness between 0.36 and 12 μm. The counter electrode was a Zn plate (5 × 3 cm^2). Next, a heat-treatment was performed at 500°C in air for different time to remove the PS microspheres, leaving the ZnO skeleton completely intact. Both electrophoresis and electroplating were conducted by Keithley 2400.

Scanning electron microscope [(SEM); Jeol JSM-6700F] was employed to observe the morphologies for the PS colloidal crystals and ZnO inverse opals. Crystallinity for the ZnO skeleton was obtained from x-ray diffraction using a Cu *K*α of 0.154 nm [(XRD);

* Electrochemical Society Active Member.
z E-mail: ppwu@mail.nctu.edu.tw

Siemens D5000]. The stoichiometry and defect states for the ZnO structure were determined via X-ray photoelectron spectroscopy [(XPS); Thermo Microlab 350] and photoluminescence measurements using a He–Cd laser at 325 nm [(PL); Kimmon IK], respectively.

Results and Discussion

In our earlier studies of Ni inverse opals, we realized that the crystallinity of the colloidal template was critical for subsequent electroplating as it affected the percolation distance for the plating electrolyte that determined the iR_E loss (R_E is the electrolyte resistance) and uniformity of the Ni deposit.[19,36] This effect is expected to become more pronounced as the ZnO is insulative in nature so both the electrolyte and electrode resistance are varied for the entire plating process. In our observations, the PS template fell apart when it did not possess sufficient thickness. On the other hand, when the PS template was too thick, the electrolyte percolation became difficult, which led to serious inconsistency in surface uniformity for the deposited ZnO. Figure 1 provides the SEM images for the PS template in both top and cross-sectional views. As shown in Fig. 1a, the PS microspheres were arranged in a hexagonal (111) lattice without the formation of vacancies as well as surface islands and valleys. This unique feature was due to the appropriate experimental design and processing parameters enabling sufficient time for the incoming PS microspheres to find the lowest energy sites so a close-pack structure was assembled in a layer-by-layer mode. This impressive packing order can be confirmed by the cross-sectional view shown in Fig. 1b, where a close-pack hexagonal lattice was clearly visible. The thickness for the PS template was 13 μm, which corresponded to 28 colloidal layers.

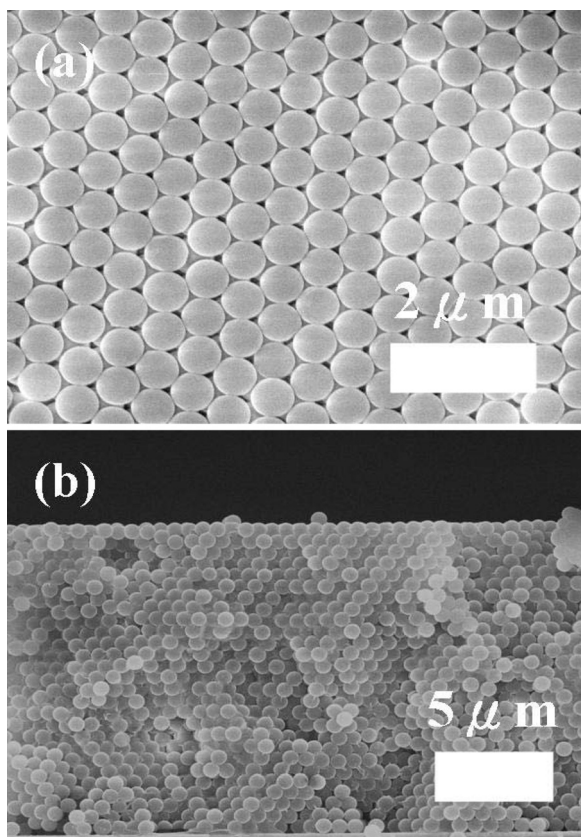In literature, the cathodic deposition of ZnO proceeds via the reduction of dissolved nitrate or oxygen, and both methods have been thoroughly studied.[38–41] In particular, to electrodeposit ZnO in the interstitial voids among the PS microspheres, the nitrate route is often adopted because its reactants and mass transport can be controlled more precisely. Unfortunately, due to the hydrophobic nature of PS template, the nitrate is usually dissolved in a mixture of ethanol and water for wetting purpose. Previously, it was suggested that the addition of ethanol promoted wetting but altered the ZnO deposit undesirably.[27] Hence, an optimized ethanol/water volume ratio of 3/7 was identified to prepare the desirable ZnO microstructure. Since we constructed the PS template with significantly reduced crystallographic defects from vertical electrophoresis, the electroplating of ZnO was expected to be less challenging. Hence, we were able to obtain a desirable ZnO structure with a lower ethanol/water volume ratio of 1/9. This potentially enabled a faster deposition rate and improved ZnO microstructure as compared to those reported earlier.

Figure 2 demonstrates the voltage profile as a function of plating time under cathodic current of 1 mA/cm^2. Since the deposition current was fixed, the recorded voltage was proportional to the sum of electrolyte resistance (electrolytic iR_E loss), electrode resistance (iR_{ZnO}, R_{ZnO} is the ZnO resistance), and charge transfer resistance for the ZnO formation (iR_{CT}, R_{CT} is the charge transfer resistance). The R_{CT} was presumed unchanged because the ZnO was deposited on the ZnO itself. Hence, the factors that affected the voltage reading were the variation in both R_E and R_{ZnO}. Apparently, the voltage experienced a sudden drop initially but rose steadily afterward. This immediate voltage drop was attributed to the incubation and formation of ZnO nuclei on the ITO substrate. Because the ZnO was not an electronic conductor, subsequent formation of ZnO increased the value of R_{ZnO}, and as a result, the voltage reading became larger gradually with deposition time. This increasing R_{ZnO} resistance counteracted the opposite effect of shorter electrolyte percolation distance that led to a smaller electrolytic iR_E. In our observation, the lowest point in the voltage profile coincided with the formation of a monolayered ZnO. After 70 min, the interstitial voids among the PS microspheres were completely filled with ZnO so random growth took place on the exterior surface, resulting in a slightly larger fluctuation in the voltage responses. In between, by selecting the necessary deposition time, we were able to produce ZnO with targeted thickness/layer.

The cross-sectional SEM pictures for the ZnO inverse opals after removing the PS template are exhibited in Fig. 3 along with their respective top-view images in insets. As shown in Fig. 3a, a monolayer ZnO inverse structure was obtained after electroplating of 3 min. The ZnO inverse structure was relatively smooth on its surface and the interstitial voids were properly arranged in a triangular lattice. In addition, the ZnO skeleton was continuous, forming a
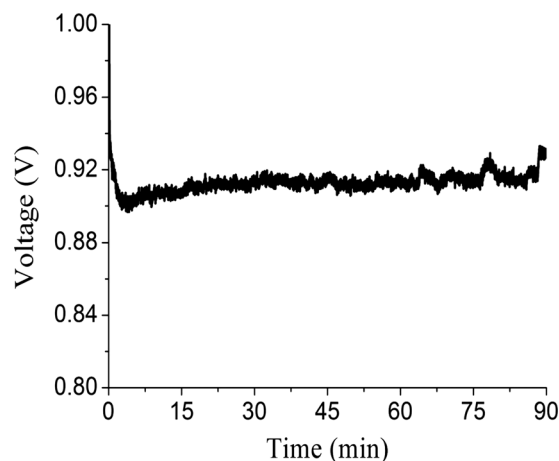

Figure 1. SEM images of the colloidal crystals after 10 min of electrophoretic deposition from the PS suspension with *p*H 8 and 10 V/cm; (a) top view and (b) side view.

Figure 2. Voltage response as a function of time during electroplating of ZnO at 1 mA/cm^2.
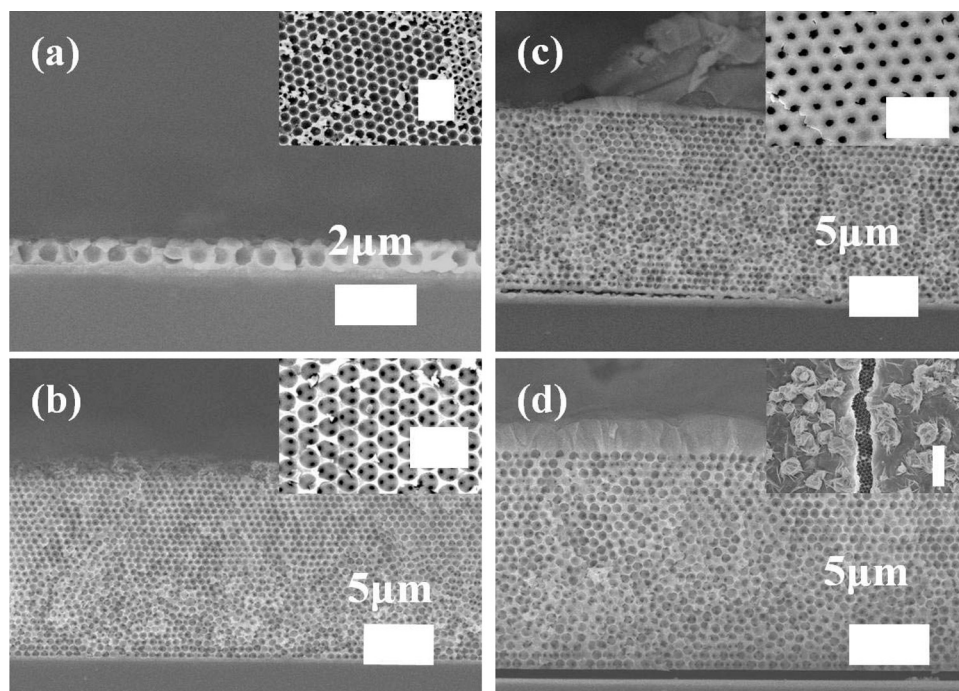
Figure 3. SEM images for ZnO inverse opals after removing PS template. The ZnO electroplating lasted for (a) 3, (b) 45, (c) 50, and (d) 90 min. The inset pictures are their top view images with scale bar of 2 µm.

periodic macroporous network. After 45 min of electroplating, shown in Fig. 3b, the ZnO inverse opals attained a thickness of 12 µm, which corresponded to 26 layers. In Fig. 3c, the ZnO inverse opals reached the top surface of PS template after 50 min of electroplating. At this stage, the ZnO skeleton became notably coarse as two-dimensional film growth was occurring. In Fig. 3d, overplating of ZnO was found, resulting in the formation of irregular ZnO crystallites on the surface. From the SEM images, the growth rate for the ZnO inverse structure was determined at 266 nm/min. Therefore, combining electrophoresis, electroplating, and heat-treatment, a large-area ZnO inverse opaline structure was successfully fabricated in less than 4.5 h. In addition, since both electrophoresis and electroplating were carried out in a solution state, structural alteration during sample transfer was likely to be negligible, rendering superb integrity and surface uniformity.

Figure 4 presents the XRD patterns for the ZnO inverse opals after heat-treatment at 500°C in air for 30, 60, and 180 min, respectively. In addition, an XRD pattern for the ZnO inverse opals prepared from the nitrate route without the addition of ethanol is shown
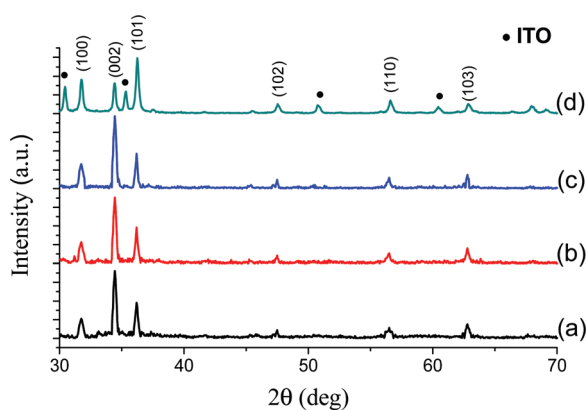
for comparison. From our observations, a heat-treatment of 30 min was adequate to remove the PS template completely leaving an integral ZnO replica with negligible structural damage. Hence, any prolonged heat-treatment was essentially an annealing process to improve the ZnO crystallinity, resulting in a moderate reduction in the diffraction noises. Apparently, the ZnO inverse opals exhibited a standard wurtzite hexagonal lattice (JCPDS 361451) with relevant diffraction peaks properly indexed. However, the relative intensity for the diffraction peaks revealed a preferred orientation in (002), which was different from the ZnO inverse opals obtained from the nitrate solution without the addition of ethanol or dissolved oxygen route.[38,41] This suggested that the plating formulation played a critical role in determining the ZnO crystallinity as the nucleation and growth of ZnO were greatly affected by the constituents in electrolyte.

It is understood that the oxygen vacancies are often found in the as-synthesized ZnO, and annealing in air is effective in reducing their number. Hence, the heat-treatment that removed the PS template in our case was expected to improve the ZnO stoichiometry simultaneously. Figure 5 displays the Zn ($2p_{3/2}$) and Zn ($2p_{1/2}$) spectra from XPS analysis, which clearly reveal strong signals around 1022.5 and 1045 eV, respectively. In addition, their peak positions were slightly shifted to higher energy once the heat-treatment was prolonged. Earlier reports by Kang et al. and Khallaf et al. suggested that the reduction of oxygen vacancies and stronger bonding of zinc and oxygen were responsible for the relocation of Zn ($2p_{3/2}$) and Zn ($2p_{1/2}$) to higher binding energy.[42,43]

Variation in the oxygen vacancies can also be ascertained from the XPS signals on O ($1s$), which is presented in Fig. 6 along with curve fitting results using Oa, Ob, and Oc, respectively. The peak positions for the ZnO inverse opals after heat-treatment of 500°C for 30, 60, and 180 min were 530.2, 534.4, and 530.5 eV, respectively. In literature, the Oa (530.2 eV), Ob (531.8 eV), and Oc (532.6 eV) were attributed to the Zn–O binding energy, O^{2-} vacancy in ZnO lattice, and adsorbed oxygen on ZnO surface.[44–46] Apparently, once the heat-treatment was prolonged, the ratio of Oa/Ob became considerably larger. In addition, the intensity of Oc was increased as well, indicating a stronger surface oxygen adsorption. These adsorbed oxygens were presumed to saturate the ZnO surface, followed by diffusion to the ZnO lattice and occupation at the
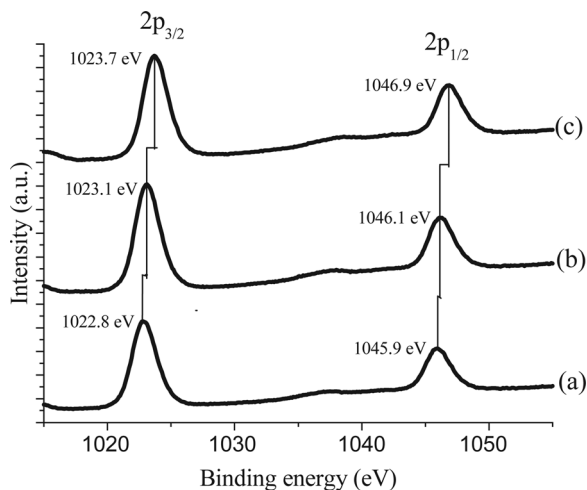

Figure 4. (Color online) XRD patterns for ZnO inverse opals after heat-treatment of 500°C for (a) 30, (b) 60, and (c) 180 min. Shown in (d) is the XRD pattern for ZnO inverse opals prepared from the nitrate route without the addition of ethanol.

Figure 5. XPS signals of Zn ($2p_{3/2}$) and Zn ($2p_{1/2}$) for ZnO inverse opals after heat-treatment of 500°C for (a) 30, (b) 60, and (c) 180 min.

O^{2-} sites. Compared to a typical ZnO thin film, the ZnO inverse skeleton not only provided a significantly larger surface area for oxygen adsorption but also enabled a shorter diffusion path, so a 30 min heat-treatment was sufficient to obtain ZnO with reduced defects.

The improved crystallinity for the ZnO inverse opals after heat-treatment is confirmed via the measurements of their PL spectra as defects in the ZnO are known to determine the intensity and position of emission signals. In general, the PL profile of ZnO contains emission spectra from both the ultraviolet and visible regimes, which are associated with band edge emission and intraband emission from impurities and defects, respectively.[1] Previously, Yang et al. reported that the PL spectra from the ZnO inverse opals were similar to that of thin film but displayed a significantly enhanced intensity.[47] They attributed the enhancement to the dielectric confinement effect as the ZnO skeleton was sandwiched by air on both sides forming a semiconductor-insulator nanostructure. Figure 7 exhibits the PL spectra for the ZnO inverse opals after different heat-treatment time. The peak positions for the ZnO inverse opals after heat-treatment of 500°C for 30, 60, and 180 min were 382, 382, and 388 nm, respectively. In addition, their intensity was decreasing with heat-treatment time. This significant reduction in the peak intensity was accompanied by a slight increase in the bandwidth. In addition to ultraviolet emission, there appeared broad visible emissions around 500 and 637 nm. The intensities for these visible emissions were much smaller as compared to what was reported earlier in similar ZnO inverse opals.[15] These emissions were moderate for samples undergoing heat-treatments of 30 and 60 min but became negligible for the sample of 180 min heat-treatment. In literature, the emissions in visible regime were likely caused by zinc vacancies (V_{Zn}), oxygen vacancy (V_O), interstitial zinc (Zn_i), interstitial oxygen (O_i), and antisite oxygen (O_{Zn}).[44] From Fig. 7, we witnessed a gradual decrease for those visible emissions, suggesting that the defective sites in the ZnO lattice were reduced considerably upon heat-treatment. This behavior was consistent with the XPS results from Figs. 5 and 6, confirming that a simple heat-treatment in air effectively improved the crystallinity and stoichiometry for the ZnO inverse opals.

An alternative explanation for the slight shift in the peak position to the longer wavelength in PL spectra is the increase of ZnO grain size upon extended heat-treatment. However, after carefully examining the XRD patterns for the ZnO inverse opals, we did not observe notable variations in the diffraction peaks. Hence, we concluded that the shift of PL peak was attributed entirely to the reduction of defects in the ZnO inverse opals after heat-treatment. In summary, combining electrophoresis, electroplating, and heat-treatment, we demonstrated the fabrication of large-area ZnO
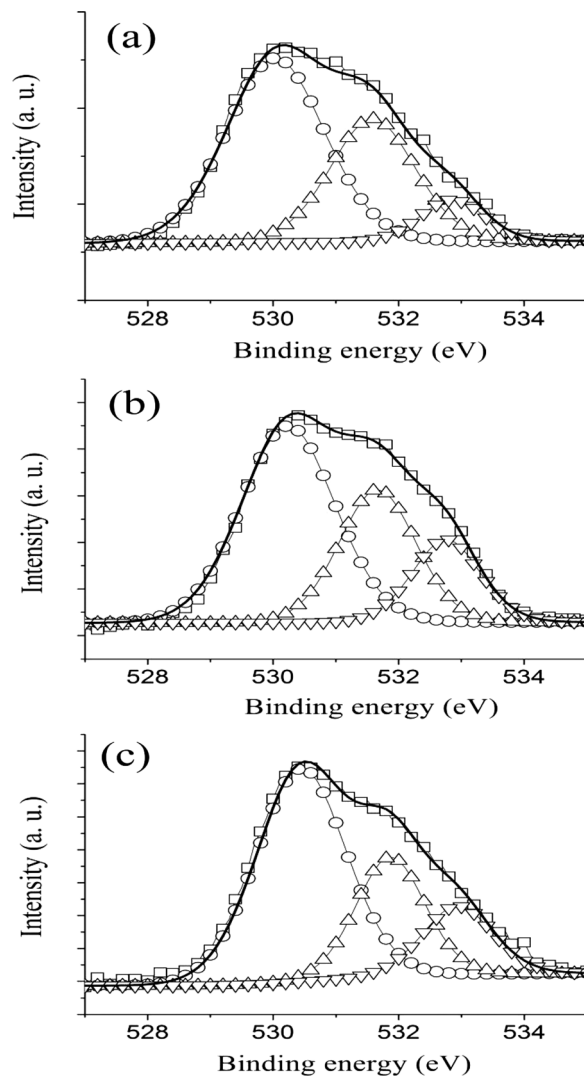

Figure 6. XPS signals of O ($1s$) in both experimental results (□) and curve fitting (—) for ZnO inverse opals after heat-treatment of 500°C for (a) 30, (b) 60, and (c) 180 min. The curve fitting is based on Oa (○), Ob (△), and Oc (▽).

inverse opals with significantly reduced crystallographic defects and desirable microstructure. These ZnO inverse opals can potentially be employed for optoelectronic applications where a well-defined bandgap is required.
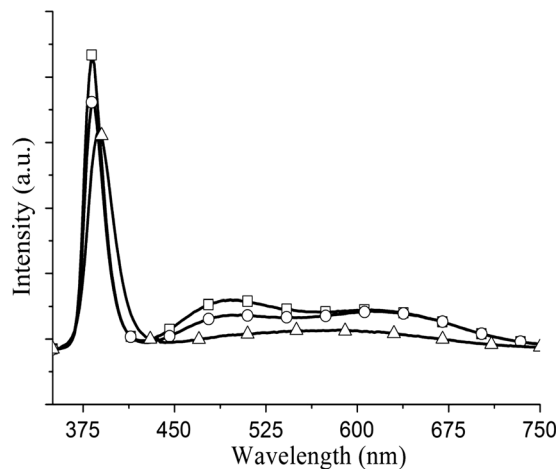

Figure 7. PL spectra for ZnO inverse opals after heat-treatment of 500°C for 30 (□), 60 (○), and 180 (△) min.

Conclusions

A facile electrochemical fabrication scheme to construct large-area ZnO inverse opals on a ITO substrate with reduced defects and controlled thickness (0.36–12 μm) was demonstrated. The PS colloidal crystals were assembled by vertical electrophoresis and employed as template for ZnO electroplating, followed by heat-treatment in air at 500°C to remove the PS microspheres. Since the PS template was prepared with significantly reduced crystallographic defects, the electroplating of ZnO was able to achieve at a reduced ethanol/water volume ratio of 1/9, leading to a faster deposition rate and improved ZnO microstructure. SEM images exhibited superior uniformity and reduced microstructural defects for the colloidal template and ZnO skeleton. XRD revealed a wurtzite hexagonal lattice with (002) preferred orientation for the ZnO inverse opals. In addition, both XPS and PL spectra indicated improved crystallinity and stoichiometry with increasing heat-treatment time. These ZnO inverse opals can potentially be employed for optoelectronic applications where well-defined bandgap is required.

Acknowledgments

References

1. A. B. Djurisic and Y. H. Leung, *Small*, **2**, 944 (2006).
2. M. K. Lee and H. F. Tu, *J. Electrochem. Soc*., **155**, D758 (2008).
3. K. Remashan, Y. S. Choi, S. J. Park, and J. H. Jang, *J. Electrochem. Soc*., **157**, H1121 (2010).
4. Y. Gao and M. Nagai, *Langmuir*, **22**, 3936 (2006).
5. C. S. Hsiao, W. L. Kuo, S. Y. Chen, J. L. Shen, C. C. Lin, and S. Y. Cheng, *J. Electrochem. Soc*., **155**, K96 (2008).
6. H. Liu, L. Feng, J. Zhai, L. Jiang, and D. Zhu, *Langmuir*, **20**, 5659 (2004).
7. A. Dorfman, N. Kumar, and J. Hahm, *Langmuir*, **22**, 4890 (2006).
8. C. L. Hsu, S. J. Chang, H. C. Hung, Y. R. Lin, C. J. Huang, Y. K. Tseng, and I. C. Chen, *J. Electrochem. Soc*., **152**, G378 (2005).
9. C. C. Lin, S. Y. Chen, and S. Y. Cheng, *Appl. Phys. Lett*., **84**, 5040 (2004).
10. M. Fu and J. Zhou, *J. Electrochem. Soc*., **157**, D450 (2010).
11. M. Gupta, D. Pinisetty, J. C. Flake, and J. J. Spivey, *J. Electrochem. Soc*., **157**, D473 (2010).
12. J. H. He, S. Singamaneni, C. H. Ho, Y. H. Lin, M. E. McConney, and V. V. Tsukruk, *Nanotechnology*, **20**, 065502 (2009).
13. Y. N. Ou, G. R. Li, Z. L. Wang, X. L. Yu, and Y. X. Tong, *J. Electrochem. Soc*., **157**, D264 (2010).
14. Y. J. Xing, Z. H. Xi, Z. Q. Xue, X. D. Zhang, J. H. Song, R. M. Wang, J. Xu, Y. Song, S. L. Zhang, and D. P. Yu, *Appl. Phys. Lett*., **83**, 1689 (2003).
15. Y. Yang, H. Yan, Z. Fu, B. Yang, and J. Zuo, *Appl. Phys. Lett*., **88**, 191909 (2006).
16. C. Lopez, *Adv. Mater*., **15**, 1679 (2003).
17. Y. A. Vlasov, X. Z. Bo, J. C. Sturm, and D. J. Norris, *Nature (London)*, **414**, 289 (2001).
18. P. Jiang, J. F. Bertone, K. S. Hwang, and V. L. Colvin, *Chem. Mater*., **11**, 2132 (1999).
19. Y. J. Huang, C. H. Lai, P. W. Wu, and L. Y. Chen, *J. Electrochem. Soc*., **157**, P18 (2010).
20. C. H. Lai, Y. J. Huang, P. W. Wu, and L. Y. Chen, *J. Electrochem. Soc*., **157**, P23 (2010).
21. P. V. Braun and P. Wiltzius, *Nature (London)*, **402**, 603 (1999).
22. P. V. Braun and P. Wiltzius, *Adv. Mater*., **13**, 482 (2001).
23. L. Xu, W. L. Zhou, C. Frommen, R. H. Baughman, A. A. Zakhidov, L. Malkinski, J. Q. Wang, and J. B. Wiley, *Chem. Commun*., **2000**, 997 (2000).
24. P. N. Bartlett, M. A. Ghanem, I. S. El Hallag, P. de Groot, and A. Zhukov, *J. Mater. Chem*., **13**, 2596 (2003).
25. P. N. Bartlett, T. Dunford, and M. A. Ghanem, *J. Mater. Chem*., **12**, 3130 (2002).
26. J. Hu, M. Abdelsalam, P. Bartlett, R. Cole, Y. Sugawara, J. Baumberg, S. Mahajan, and G. Denuault, *J. Mater. Chem*., **19**, 3855 (2009).
27. H. Yan, Y. Yang, Z. Fu, B. Yang, L. Xia, S. Fu, and F. Li, *Electrochem. Commun*., **7**, 1117 (2005).
28. A. Stein, F. Li, and N. R. Denny, *Chem. Mater*., **20**, 649 (2008).
29. M. Scharrer, X. Wu, A. Yamilov, H. Cao, and R. P. H. Chang, *Appl. Phys. Lett*., **86**, 151113 (2005).
30. H. Yan, C. F. Blanford, B. T. Holland, W. H. Smyrl, and A. Stein, *Chem. Mater*., **12**, 1134 (2000).
31. S. M. Abrarov, S. U. Yuldashev, S. B. Lee, and T. W. Kang, *J. Lumin*., **109**, 25 (2004).
32. V. V. Ursaki, I. M. Tiginyanu, V. V. Zalamai, V. M. Masalov, E. N. Samarov, G. A. Emelchenko, and F. Briones, *J. Appl. Phys*., **96**, 1001 (2004).
33. B. H. Juarez, P. D. Garcia, D. Golmayo, A. Blanco, and C. Lopez, *Adv. Mater*., **17**, 2761 (2005).
34. Y. W. Chung, I. C. Leu, J. H. Lee, and M. H. Hon, *Electrochim. Acta*, **54**, 3677 (2009).
35. Y. J. Huang, C. H. Lai, and P. W. Wu, *Electrochem. Solid-State Lett*., **11**, P20 (2008).
36. Y. J. Huang, C. H. Lai, P. W. Wu, and L. Y. Chen, *Mater. Lett*., **63**, 2393 (2009).
37. C. E. Reese and S. A. Asher, *J. Colloid Interface Sci*., **248**, 41 (2002).
38. M. Izaki and T. Omi, *J. Electrochem. Soc*., **144**, 1949 (1997).
39. K. H. Yeo, L. K. Teh, and C. C. Wong, *J. Cryst. Growth*, **287**, 180 (2006).
40. S. Peulon and D. Lincot, *J. Electrochem. Soc*., **145**, 864 (1998).
41. A. I. Inamdar, S. H. Mujawar, S. B. Sadale, A. C. Sonavane, M. B. Shelar, P. S. Shinde, and P. S. Patil, *Sol. Energy Mater. Sol. Cells*, **91**, 864 (2007).
42. S. J. Kang, Y. H. Joung, H. H. Shin, and Y. S. Yoon, *J. Mater. Sci.: Mater. Electron*., **19**, 1073 (2008).
43. H. Khallaf, G. Chai, O. Lupan, H. Heinrich, S. Park, A. Schulte, and L. Chow, *J. Phys. D: Appl. Phys*., **42**, 135304 (2009).
44. P. T. Hsieh, Y. C. Chen, K. S. Kao, and C. M. Wang, *Appl. Phys. A*, **90**, 317 (2008).
45. K. R. Murali, *J. Phys. Chem. Solids*, **68**, 2293 (2007).
46. Y. S. Kim, W. P. Tai, and S. J. Shu, *Thin Solid Films*, **491**, 153 (2005).
47. Y. Yang, H. Yan, Z. Fu, B. Yang, J. Zuo, and S. Fu, *Solid State Commun*., **139**, 218 (2006).